

Emergence of large spin-charge interconversion at an oxidized Cu/W interface

Inge Groen ¹, Van Tuong Pham ², Stefan Ilić ³, Andrey Chuvilin ^{1,4}, Won Young Choi ¹, Ederne Sagasta ¹,
 Diogo C. Vaz ¹, Isabel C. Arango ¹, Nerea Ontoso ¹, F. Sebastian Bergeret ^{3,5}, Luis E. Hueso ^{1,4},
 Ilya V. Tokatly ^{4,5,6} and Fèlix Casanova ^{1,4}

¹*CIC nanoGUNE BRTA, 20018 Donostia-San Sebastian, Basque Country, Spain*

²*IMEC, 3001 Leuven, Belgium*

³*Centro de Física de Materiales (CFM-MPC), Centro Mixto CSIC-UPV/EHU, 20018 Donostia-San Sebastian, Basque Country, Spain*

⁴*IKERBASQUE, Basque Foundation for Science, 48009 Bilbao, Basque Country, Spain*

⁵*Donostia International Physics Center (DIPC), 20018 Donostia-San Sebastian, Basque Country, Spain*

⁶*Nano-Bio Spectroscopy Group and European Theoretical Spectroscopy Facility (ETSF), Departamento de Polímeros y Materiales Avanzados: Física, Química y Tecnología, Universidad del País Vasco, 20018 Donostia-San Sebastián, Basque Country, Spain*



(Received 6 November 2022; revised 30 January 2023; accepted 27 April 2023; published 23 May 2023)

Spin-orbitronic devices can integrate memory and logic by exploiting spin-charge interconversion (SCI), which is optimized by design and materials selection. In these devices, interfaces are crucial elements as they can prohibit or promote spin flow in a device as well as possess spin-orbit coupling resulting in interfacial SCI. Therefore, investigation of interfaces in spin-orbitronic devices is important. Here, we study the origin of SCI in a Py/Cu/W lateral spin valve and quantify its efficiency. An exhaustive characterization of the interface between Cu and W electrodes uncovers the presence of an oxidized layer (WO_x). We determine that the SCI occurs at the Cu/ WO_x interface with a temperature-independent interfacial spin-loss conductance of $G_{\parallel} \approx 20 \times 10^{13} \Omega^{-1} \text{m}^{-2}$ and an interfacial spin-charge conductivity $\sigma_{\text{SC}} = -1600 \Omega^{-1} \text{cm}^{-1}$ at 10 K ($-800 \Omega^{-1} \text{cm}^{-1}$ at 300 K). This corresponds to an efficiency given by the inverse Edelstein length $\lambda_{\text{IEE}} = -0.8 \text{ nm}$ at 10 K (-0.4 nm at 300 K), which is remarkably larger than in metal/metal and metal/oxide interfaces and bulk heavy metals. The large SCI efficiency at such an oxidized interface makes it a promising candidate for the magnetic readout in MESO logic devices.

DOI: [10.1103/PhysRevB.107.184438](https://doi.org/10.1103/PhysRevB.107.184438)

I. INTRODUCTION

In the field of spin orbitronics, great efforts have been made to develop theories and device architectures that allow technological advancements in digital information storage and computation. These developments include writing and reading of information in magnetic states to achieve scalable and energy-efficient nonvolatile memory such as spin-orbit torque magnetoresistive random access memory (SOT-MRAM) [1,2]. Now, the field is pushing even further with proposals for spin-orbit logic [3]. These devices rely on spin-orbit coupling (SOC) which permits spin-charge interconversion (SCI), that is, the conversion of a spin current density into a charge current density or vice versa. Such conversion can take place in bulk materials (3D) via the spin Hall effect [4] and at interfaces (2D) via the Rashba-Edelstein effect [5–12], and in specific systems, both bulk and interfacial SCI are observed [13,14]. Spin-orbit devices benefit from spin-orbit materials (SOMs) providing high SCI efficiencies. For optimization of these efficiencies, it is important to distinguish between bulk and interfacial SCI, which is not straightforward since interfaces are present in most devices.

Lateral spin valve (LSV) devices can be used for SCI measurements in both 2D and 3D systems [10,12,15,16]. The nonlocal geometry of this device allows separating pure spin current from charge current such that spurious effects arising from the latter are eliminated from the detected signal. Two

independent configurations help to determine the spin diffusion length (λ) and the SCI efficiency of a SOM. However, the spin transport at the interface of the channel and SOM electrode remains an issue. Lately, the importance of interfaces has been pointed out by several works [17–20] where the interface can reduce or even prevent spin sink into SOM, or possess 2D SCI due to interfacial SOC. Hence, the quantification of the 3D SCI in the SOM might be affected by the presence of an interface.

Here, we study SCI in an all-metallic Py/Cu/W LSV. Electrical measurements of the Cu/W interface supported by scanning transmission electron microscopy (STEM) images reveal that the interface resistance originates from an oxide layer created during the fabrication of the device. After analyses of different spin transport scenarios in the system, we identified that the SCI occurs at the Cu/oxide interface. We find a temperature-independent interfacial spin-loss conductance ($G_{\parallel} \approx 20 \times 10^{13} \Omega^{-1} \text{m}^{-2}$) and a spin-charge conductivity of $\sigma_{\text{SC}} = -800 \Omega^{-1} \text{cm}^{-1}$ at 300 K, corresponding to an inverse Edelstein length $\lambda_{\text{IEE}} = -0.4 \text{ nm}$ at 300 K for the Cu/oxide interface. The high resistivity and large SCI in this system is promising for developing the magnetic-state readout in the magnetoelectric spin-orbit (MESO) logic device [21,22]. Even more, this work highlights the importance of studying every aspect of all-metallic devices carefully, in particular the interface, to extract meaningful spin relaxation and SCI efficiency parameters.

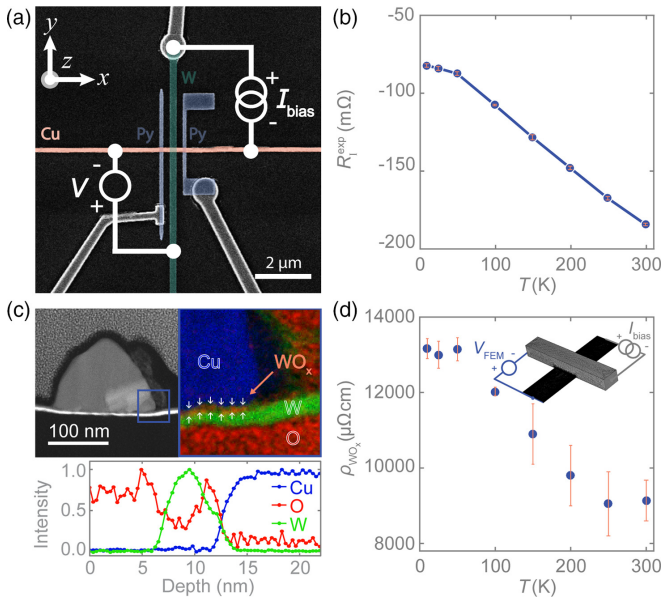


FIG. 1. Characterization of the Cu/W interface. (a) A false-color SEM image of a Py/Cu/W LSV with the Py, Cu, and W electrodes indicated by blue, orange, and green, respectively. The electrical configuration presents the four-probe interface resistance measurement of the Cu/W interface. (b) Temperature dependence of the experimental interface resistance R_I^{exp} of the Cu/W interface. (c) A STEM image and EDX analysis of the Cu/W interface. Top left panel: HAADF STEM image of a cross section of the Cu/W interface area. Top right panel: False-colored EXD map of the blue square on the STEM image. The false colors correspond to O (red), Cu (blue), and W (green). An interfacial oxide layer is indicated by white arrows. Bottom panel: Compositional analysis of the EDX map showing the Cu, O, and W as a function of the depth, indicating the presence of a WO_x layer in between the Cu and W electrodes. (d) The resistivity of the WO_x layer as a function of the temperature, extracted from the 3D FEM simulation in combination with R_I^{exp} . Inset: the geometrical model and measurement configuration in the 3D FEM simulation.

II. EXPERIMENTAL DETAILS

The Py/Cu/W LSV consists of two parallelly aligned Py electrodes and a W electrode placed in between the Py electrodes. These three electrodes are connected by a transverse Cu channel. Figure 1(a) displays a top-view scanning electron microscopy (SEM) image of the device. The devices are fabricated on SiO_2 (150 nm)/Si substrates in three steps, each step involving electron-beam lithography (EBL), metal deposition, and a lift-off process. The first step includes EBL of the Py nanostructure, followed by Py deposition via e -beam evaporation (rate $\sim 0.56 \text{ \AA s}^{-1}$ and $p_{\text{dep}} \sim 2.3 \times 10^{-8}$ Torr). In a second EBL step, the nanostructure for the W is defined with subsequent deposition of W by magnetron sputtering (rate $\sim 0.11 \text{ \AA s}^{-1}$, $p_{\text{Ar}} = 3 \text{ mTorr}$, $P = 10 \text{ W}$, $p_{\text{base}} \sim 2 \times 10^{-8}$ Torr at room temperature). After lift-off, Ar-ion-beam milling is performed at grazing incidence to remove sharp vertical edges from the Py and W electrodes formed by materials deposited on the walls of the resists which did not detach from the electrodes during the lift-off process. Lastly, the Cu nanostructures are defined by EBL. Before the deposition of Cu, Ar-ion-beam milling is

performed at normal incidence to clean the Py and W surfaces from resist residues and oxidation. Next, 3 nm of Cu are *in situ* deposited by magnetron sputtering (rate $\sim 1.88 \text{ \AA s}^{-1}$, $p_{\text{Ar}} = 3 \text{ mTorr}$, $P = 250 \text{ W}$, $p_{\text{base}} \sim 3 \times 10^{-6}$ Torr at room temperature) in an attempt to protect Py and especially W from reoxidation before transferring the sample to an UHV evaporation chamber, where high quality Cu (low resistivity and long spin diffusion length) is grown. This Cu is deposited by thermal evaporation (rate $\sim 1.5 \text{ \AA s}^{-1}$ and $p_{\text{dep}} \sim 1.3 \times 10^{-8}$ Torr) and subsequently lifted off in acetone. Finally, the sample is capped with a magnetron sputtered 5-nm-thick film of SiO_2 (rate $\sim 0.5 \text{ \AA s}^{-1}$, $p_{\text{Ar}} = 3 \text{ mTorr}$, $P = 200 \text{ W}$, $p_{\text{base}} \sim 2 \times 10^{-8}$ Torr at room temperature).

The width (w) and thickness (t) of the electrodes for the device used in this study are $w_{\text{Py}} = 124 \text{ nm}$, $t_{\text{Py}} = 30 \text{ nm}$, $w_{\text{W}} = 195 \text{ nm}$, $t_{\text{W}} = 4.5 \text{ nm}$, $w_{\text{Cu}} = 123 \text{ nm}$, and $t_{\text{Cu}} = 90 \text{ nm}$. The measured resistivities of the different electrodes are presented in Supplemental Material S1 [23]. The behavior of the W resistivity indicates that the β phase, which possesses large SCI, is dominant [24]. The transport measurements are carried out in a physical property measurement system (PPMS) from Quantum Design. We can apply an in-plane magnetic field and the electrical measurements are performed using the “dc reversal technique” with a Keithley 2182 nanovoltmeter and 6221 current source.

III. RESULTS AND DISCUSSION

A. Interface resistance

The four-point measurement configuration in the LSV device presented in Fig. 1(a) can be used for probing the experimental interface resistance R_I^{exp} . Figure 1(b) shows the resulting interface resistance at various temperatures. R_I^{exp} is observed to be negative. This negative value for interface resistance is an artifact that comes from an inhomogeneous current density flow and voltage drop is facilitated by a low-impedance interface [25,26]. 3D finite element method (FEM) simulations are utilized to extract the actual interface resistance.

STEM has been performed to investigate the W and Cu channels at the interface region and to accordingly define the geometrical model within the 3D FEM resembling the Cu and W electrodes. Figure 1(c) shows a cross-sectional STEM image of the Cu/W interface. The element composition is inspected by energy dispersive x-ray (EDX) analysis in the area indicated by the blue square. The observed elements in this region are oxygen (O), W, and Cu. Surprisingly, O appears in between the Cu and W electrodes. Supplemental Material S2 contains a deeper discussion on the elemental composition [23]. We find the W electrode thickness below the Cu channel to be 2.8 nm thick. The oxide layer, clearly visible in the zoom of the blue square indicated by white arrows, has an average thickness of $\sim 1.5 \text{ nm}$ and consists of W and O (for a detailed discussion on the stoichiometry of the oxide layer, see Supplemental Material S3 [23]). In the remainder of this paper, we will refer to this layer as the oxide layer and use the tag “ WO_x .”

The finite thickness of the oxide layer means that the interface in the 3D FEM simulation cannot be considered

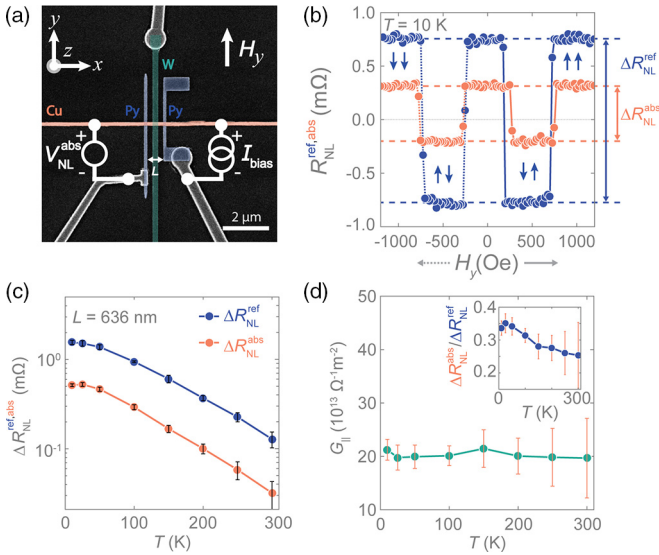


FIG. 2. Spin absorption in the Py/Cu/W LSV. (a) A false-color SEM image presenting a top view of the Py/Cu/W LSV including the spin absorption technique measurement configuration. The magnetic field is applied along the easy axis of the Py electrodes. (b) The nonlocal resistance for the reference LSV (blue) and the LSV with the middle W electrode (orange) at 10 K. The difference between the low and high resistance state gives the spin signals $\Delta R_{\text{NL}}^{\text{ref}}$ and $\Delta R_{\text{NL}}^{\text{abs}}$ for the associated LSVs. (c) The spin signals $\Delta R_{\text{NL}}^{\text{ref}}$ and $\Delta R_{\text{NL}}^{\text{abs}}$ at different temperatures. (d) The temperature dependence of the interfacial spin-loss conductance G_{\parallel} obtained from applying Eq. (2) to $\Delta R_{\text{NL}}^{\text{abs}}/\Delta R_{\text{NL}}^{\text{ref}}$ which is displayed in the inset.

as a boundary condition, but the geometrical model must contain an additional layer with its own materials properties. The geometry has been constructed considering the structural details found in the TEM images (Supplemental Material S2 [23]). Although the thickness of the W electrode underneath the Cu channel and away from the Cu channel is different, we consider the resistivity of the W electrode to be the same everywhere. The electrical configuration in the simulation is shown in the inset of Fig. 1(d) [and is the same as presented in Fig. 1(a)]. The voltage is probed while varying the resistivity of the oxide layer ρ_{WO_x} . The resistance for which the FEM resistance R_{FEM} is equal to $R_{\text{I}}^{\text{exp}}$ gives the correct ρ_{WO_x} (see Supplemental Material S4 for more details [23]). Note that the described method can also be used when there is no interfacial oxide layer by replacing the finite layer by a contact impedance and the resistivity by an interface resistance. Figure 1(d) graphs the resulting temperature dependence of ρ_{WO_x} which is relatively high compared to resistivities in the metal electrodes (Supplemental Material S1 [23]) and is considered in the following studies on the spin absorption and SCI.

B. Spin absorption

The spin absorption technique is used for defining λ of materials such as ferromagnets and SOMs with short λ . Figure 2(a) displays the SEM image of our LSV with the measurement configuration for the spin absorption technique. A bias current I_{bias} is applied from the Cu channel into the Py

electrode creating a spin accumulation at the Py/Cu interface. Spin diffusion in the Cu channel away from the interface region results in a pure spin current (on the side where I_{bias} does not flow). A second Py electrode is used to detect this spin current. The W electrode positioned in between the two Py electrodes can absorb part of the spin current flowing in the Cu channel depending on spin properties of the W and WO_x layers, and the W/ WO_x and Cu/ WO_x interfaces.

Figure 2(b) plots the magnetic field dependence of the nonlocal resistance ($R_{\text{NL}} = V_{\text{NL}}/I_{\text{bias}}$) in a reference LSV without the W electrode ($R_{\text{NL}}^{\text{ref}}$) and the LSV with the W electrode ($R_{\text{NL}}^{\text{abs}}$) at 10 K. The two Py electrodes are designed in such a way that the magnetic switching fields are different. Therefore, the parallel and antiparallel resistance states can be identified by parallelly aligning the ferromagnetic metal (FM) with an external magnetic field and then sweeping this field [15,16]. The difference between the resistance of the parallel and antiparallel configuration gives the spin signals $\Delta R_{\text{NL}}^{\text{ref}}$ and $\Delta R_{\text{NL}}^{\text{abs}}$. Figure 2(b) shows that $\Delta R_{\text{NL}}^{\text{abs}}$ is smaller than $\Delta R_{\text{NL}}^{\text{ref}}$, meaning that the W electrode with the interfacial WO_x layer allows for spin absorption. Figure 2(c) presents the temperature dependence of the spin signals. The observed $\Delta R_{\text{NL}}^{\text{abs}}$ is of the same order of magnitude as other all-metallic LSVs based on Nb [15], Pt [16], Ta [27], CuIr [28], CuBi [29], or AuW [30] electrodes or even by an electrode constructed out of metallic/oxide heterostructures [10].

The value of λ in a SOM using the spin absorption technique is typically obtained in devices with a transparent interface between the spin transport channel of a nonmagnetic metal (NM) and a SOM electrode. However, in LSVs with resistive interfaces, that is, LSVs in which the spin resistance of the interface is dominant over the one of SOM, the spin properties of the SOM cannot be accessed and only the interfacial properties can be explored. Interestingly, spins are being absorbed in our Py/Cu/W LSV even though the Cu/W contains a resistive interfacial oxide layer. The ratio of the spin signals $\eta = \Delta R_{\text{NL}}^{\text{abs}}/\Delta R_{\text{NL}}^{\text{ref}}$ is used to pinpoint where the spins are absorbed and elucidate the spin properties that are probed. We assume that the measured interface resistance comes from the oxide resistivity and the W/ WO_x and Cu/ WO_x interfaces are transparent, as we cannot differentiate the contribution of each candidate to the experimental interface resistance. Then, η for bulk and interfacial dominant spin absorption are respectively given by

$$\eta_{\text{bulk}} = \left[1 + \frac{G_{\text{s}}^{\text{SOM}}}{G_{\text{s}}^{\text{NM}}} \left(\frac{1}{2} - \frac{1}{1 + r_{\text{FM}} e^{L/\lambda_{\text{NM}}}} \right) \right]^{-1}, \quad (1)$$

and

$$\eta_{\text{interfacial}} = \left[1 + \frac{G_{\parallel} A_{\text{I}}}{G_{\text{s}}^{\text{NM}}} \left(\frac{1}{2} - \frac{1}{1 + r_{\text{FM}} e^{L/\lambda_{\text{NM}}}} \right) \right]^{-1}, \quad (2)$$

with $r_{\text{FM}} = 1 + 2G_{\text{s}}^{\text{NM}}/G_{\text{s}}^{\text{FM}}$ where the spin conductance for the NM channel $G_{\text{s}}^{\text{NM}} = A_{\text{NM}}/\rho_{\text{NM}}\lambda_{\text{NM}}$, the FM electrode $G_{\text{s}}^{\text{FM}} = (1 - P^2)A_{\text{FM}}/\rho_{\text{FM}}\lambda_{\text{FM}}$, and the SOM electrode $G_{\text{s}}^{\text{SOM}} = A_{\text{SOM}}/\rho_{\text{SOM}}\lambda_{\text{SOM}}$ with A being the cross-sectional area through which the spin current flows in the associate electrode, and P is the polarization of the FM electrode. G_{\parallel} is the interfacial spin-loss conductance and A_{I} is the NM/SOM interface area. The derivation of η for the total spin

TABLE I. Summary of the interfacial spin absorption and spin-charge interconversion in different interfaces. The spin absorption is given by the interfacial spin-loss conductance G_{\parallel} and the SCI by the interfacial spin-charge conductivity σ_{SC} . The inverse Edelstein length λ_{IEE} is defined as $\sigma_{SC}/G_{\parallel}$.

| Materials system | T (K) | G_{\parallel} [$10^{13} \Omega^{-1} \text{m}^{-2}$] | σ_{SC} ($\Omega^{-1} \text{cm}^{-1}$) | λ_{IEE} (nm) | Ref. |
|---------------------|---------|---|--|----------------------|-----------|
| Cu/BiO _x | 10 | 2.8 ± 0.2 | 44 ± 8 | 0.16 ± 0.03 | [10] |
| Cu/Au | 10 | 7.6 ± 0.6 | -127 ± 8 | -0.17 ± 0.04 | [12] |
| | 300 | 9.8 ± 0.6 | -30 ± 8 | -0.03 ± 0.02 | [12] |
| Cu/WO _x | 10 | 21 ± 2 | -1600 ± 200 | -0.8 ± 0.1 | this work |
| | 300 | 20 ± 7 | -800 ± 300 | -0.4 ± 0.2 | this work |

absorption including both bulk and interfacial absorption is shown in Supplemental Material S5 [23]. Equation (1) agrees with previous derivations of bulk SCI [15,31]. The spin properties of the FM and NM channels needed for further analyses with Eqs. (1) and (2) are presented in Supplemental Material S6 [23].

The spin absorption in our device can be due to spin relaxation within the W electrode, the W/WO_x interface, the WO_x layer, or the Cu/WO_x interface. If the interface resistance is ignored and the Cu/W interface is assumed to be transparent, the resulting λ for W (~ 1.5 nm) would be comparable to values reported in other studies [32,33]. However, a careful analysis of the spin diffusion equation, considering the finite interface resistance measured, indicates that the spin absorption is dominated by the oxide layer (see Supplemental Material S7 [23]). This shows the importance of proper characterization of the active interfaces in spintronic devices. The remaining question is now whether the absorption occurs in the “bulk” oxide layer or at the Cu/WO_x interface. The absorption in the “bulk” oxide means that the spin current decays up to a certain depth $\leq t_{WO_x}$ within the oxide layer. We use Eq. (1) supposing that the oxide layer, with resistivity ρ_{WO_x} [Fig. 1(d)], is the SOM and the W just functions as a metallic electrode. λ_{WO_x} is found to be ~ 0.04 nm (see Supplemental Material S7 [23]) which is smaller than the interatomic distance of typical transition metal oxides, excluding bulk absorption in the oxide layer.

Consequently, the spin absorption must take place at the Cu/WO_x interface and Eq. (2) must be used. Equation (2) is equivalent to Eq. (1) with the spin-loss conductance $G_{\parallel}A_I$ replacing the spin conductance G_s^{SOM} (which depends on λ_{SOM}). Figure 2(d) presents G_{\parallel} in our Py/Cu/W LSV obtained from $\Delta R_{NL}^{abs}/\Delta R_{NL}^{ref}$ at different temperatures [see inset of Fig. 2(d)]. Table I compares the resulting G_{\parallel} at the Cu/WO_x interface to Cu/BiO_x [10] and Cu/Au [12] interface, which are analyzed by the same method. G_{\parallel} at the Cu/WO_x interface ($\sim 20 \times 10^{13} \Omega^{-1} \text{m}^{-2}$ at all temperatures) is remarkably larger than the ones observed in Cu/BiO_x and Cu/Au.

C. Spin-charge interconversion

Next, we investigate if the spins absorbed at the Cu/WO_x interface display interfacial SCI. Figure 3(a) shows the SEM image of the Py/Cu/W LSV, this time depicted together with the charge-to-spin measurement configuration. The bias current I_{bias} is applied through the W electrode. If the Cu/WO_x interface contains any mechanism resulting in SCI, this charge current along the interface will create a spin accumulation

which will diffuse into the Cu channel as a pure spin current. The magnetization of the Py electrode that is used to probe such spin current, by measuring a voltage between the Py and Cu electrodes (V_{SC}), is controlled by an external magnetic field (H_x) parallel to the polarization of the spin current.

Figure 3(b) presents the spin-charge resistance $R_{SC} (= V_{SC}/I_{bias})$ as a function of H_x for different temperatures between 10 and 300 K. By sweeping H_x , a change in R_{SC} is observed at all temperatures, indicating the occurrence of charge-to-spin conversion. The difference between the low and high resistance, $2\Delta R_{SC}$, is called the spin-charge signal. The inset of Fig. 3(c) plots the temperature dependence of $2\Delta R_{SC}$ that is described (for the derivation,

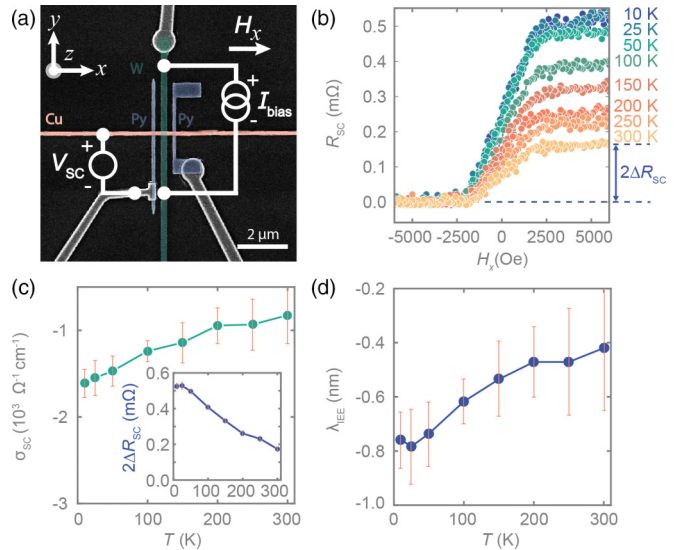


FIG. 3. Charge-to-spin conversion at the Cu/WO_x interface. (a) A false-color SEM image of the Py/Cu/W LSV and the charge-to-spin conversion measurement configuration. The external magnetic field is oriented in the x direction. (b) The magnetic field dependence of the spin-charge resistance R_{SC} for various temperatures. R_{SC} is the average of the magnetic field trace and retrace. An offset is added to R_{SC} such that the low resistance state is zero. The difference between the low and high resistance state is the spin-charge signal $2\Delta R_{SC}$. (c) The temperature dependence of the interfacial spin-charge conductivity σ_{SC} for the Cu/WO_x calculated with Eq. (3) combined with the obtained values for ΔR_{SC} , G_{\parallel} , and x_{WO_x} . Inset: Spin-charge signal as a function of temperature. (d) The temperature dependence of inverse Edelstein length λ_{IEE} resulting from the ratio between σ_{SC} and G_{\parallel} .

see Supplemental Material S8 [23]) by

$$\Delta R_{\text{SC}} = x_{\text{WO}_x} \frac{w_{\text{NM}} \sigma_{\text{SC}}}{t_{\text{WO}_x} \sigma_{\text{WO}_x}} \frac{G_s^{\text{NM}}}{G_s^{\text{FM}} G_{\parallel} A_{\text{I}}} \frac{4P e^{L/2\lambda_{\text{NM}}}}{r_{\text{FM}} r_{\parallel} e^{L/\lambda_{\text{NM}}} + r_{\parallel} - 2}, \quad (3)$$

where $r_{\parallel} = 1 + 2G_s^{\text{NM}}/G_{\parallel} A_{\text{I}}$ and σ_{SC} is the interfacial spin-charge conductivity which is the equivalent of the spin Hall conductivity for the bulk SCI. The electrical shunting factor x_{WO_x} is essential for the evaluation of SCI in the LSV as it defines the charge current flowing along the interface. This is especially critical in our LSV, in which we have a structure of three different materials with a range of resistivities. The shunting factor of the Cu/WO_x interface is assessed using 3D FEM simulations. Supplemental Material S9 [23] presents the details of electrical shunting in our device and the simulation to acquire the shunting factor.

We obtain σ_{SC} by employing Eq. (3) and using the gathered values ΔR_{SC} , G_{\parallel} and x_{WO_x} . Figure 3(c) shows a σ_{SC} value of $-1600 \Omega^{-1} \text{cm}^{-1}$ at 10 K that decreases to $-800 \Omega^{-1} \text{cm}^{-1}$ at 300 K. In this work we present one particular device, but the SCI has been observed in other devices with slightly different dimensions. The spin-charge signal is on the same order of magnitude in all devices as can be seen in Supplemental Material S10 [23], evidencing the reproducibility of the measured SCI. Such SCI requires the presence of SOC at the interface [8], which in our case is given by the heavy element W in the oxide layer. An oxide layer based on a light metal is thus not expected to show any relevant SCI. Indeed, a control experiment performed in a Py/Cu/SiO₂ LSV does not show any SCI (see Supplemental Material S11 [23]). Finally, Table I indicates that σ_{SC} of the Cu/WO_x interface is notably higher compared to the ones obtained in the Cu/BiO_x and Cu/Au systems. Remarkably, the observed σ_{SC} is comparable to σ_{SH} of Pt ($\sim 1600 \Omega^{-1} \text{cm}^{-1}$) [16].

Finally, we can combine the results of the interfacial spin-loss conductance (G_{\parallel}) and the interfacial spin-charge conductivity (σ_{SC}) to calculate the commonly used inverse Edelstein length λ_{IEE} for the Cu/WO_x interface. The resulting λ_{IEE} , -0.8 and -0.4 nm at 10 and 300 K, respectively, are significantly larger than the ones observed in Cu/BiO_x and Cu/Au at the same temperature (Table I) and $\theta_{\text{SH}} \lambda$ in Pt [16]. Note that it is more convenient to display the interfacial spin-loss and SCI parameters as G_{\parallel} and σ_{SC} because these are independent of the microscopic mechanisms leading to interfacial SCI (Rashba, spin-orbit filtering, etc.) and can be easily expanded to the 3D counterparts as G_{\parallel} and σ_{SC} are equivalent to the spin conductance of the SOM (G_{SOM}) and spin Hall conductivity (σ_{SH}) for bulk SCI, respectively. Furthermore, σ_{SC} accounts for the Onsager reciprocity of the SCI at interfaces [10]. Figure 3(d) graphs $\lambda_{\text{IEE}} = \sigma_{\text{SC}}/G_{\parallel}$ as a function of temperature, showing a decrease of this parameter with increasing temperature similar to the behavior observed in the Cu/BiO_x and Cu/Au systems.

Our device was not fabricated to study the interfacial SCI of a Cu/WO_x interface, but large SCI efficiencies that are discussed to be of interfacial origin are also observed in

spin-orbit torque studies on W/CoFe [33] and CoFe/WO_x structures [34]. Additionally, enhanced SCI efficiencies are observed in CuW alloys [35] and highly efficient SCI is measured in Cu/AlO_x interfaces [36] using spin-torque ferromagnetic resonance. The lack of heavy elements in this Cu/AlO_x structure suggests SCI mediated through orbital transport. This type of orbital Hall effect and orbital Edelstein effect could also occur in our Cu/WO_x structure.

IV. CONCLUSIONS

We studied a Py/Cu/W LSV to investigate the spin-charge interconversion properties of W. A careful analysis leads to the discovery of an oxide layer at the Cu/W interface with a high resistivity that prevents spin absorption into the W electrode. We observe that the spin absorption happens at the Cu/WO_x interface with a temperature-independent interfacial spin-loss conductance of $G_{\parallel} \approx 20 \times 10^{13} \Omega^{-1} \text{m}^{-2}$. Additionally, a large interfacial SCI is observed, with σ_{SC} varying from -1600 to $-800 \Omega^{-1} \text{cm}^{-1}$ for the temperature range from 10 to 300 K. The system has an efficiency given by the inverse Edelstein length λ_{IEE} that ranges from -0.8 nm (10 K) to -0.4 nm (300 K), which is substantially larger than other metallic interfaces [10,12] or even Pt [16]. The large SCI efficiency in the Cu/WO_x interface could be applicable to the proposed MESO logic device [21,22]. Importantly, our study indicates that one must characterize interfaces carefully when studying the spin transport properties of spin-orbit materials in nanodevices.

ACKNOWLEDGMENTS

This work was supported by Intel Corporation through the Semiconductor Research Corporation under MSR-INTEL TASK 2017-IN-2744 and the “FEINMAN” Intel Science Technology Center, and by the Spanish MICINN under the Maria de Maeztu Units of Excellence Programme (Grants No. MDM-2016-0618 and No. CEX2020-001038-M) and under Projects No. RTI2018-094861-B-I00, No. PID2020-117671GB-I00, No. PID2020-112811GB-I00, No. PID2021-122511OB-I00, PID2020-114252GB-I00 (SPIRIT), and TED2021-130292B-C42. W.Y.C. acknowledges a postdoctoral fellowship support from the “Juan de la Cierva Formación” program by the Spanish MICINN (Grant No. FJC 2018-038580-I). E.S. thanks the Spanish MECD for a Ph.D. fellowship (Grant No. FPU14/03102). D.C.V. acknowledges support from the European Commission for a Maria Skłodowska-Curie individual fellowship (Grant No. 892983-SPECTER). N.O. thanks the Spanish MICINN for a Ph.D. fellowship (Grant No. BES-2017-07963). The work of S.I. and F.S.B. was supported by European Union Horizon 2020 Research and Innovation Framework Programme under Grant No. 800923 (SUPERTED). I.V.T. and F.S.B. acknowledges support by Grupos Consolidados UPV/EHU del Gobierno Vasco (Eusko Jaularitzza) (Grants No. IT1249-19 and No. IT-1591-22). F.S.B. acknowledges financial support by the A. v. Humboldt Foundation.

- [1] A. Manchon, J. Železný, I. M. Miron, T. Jungwirth, J. Sinova, A. Thiaville, K. Garello, and P. Gambardella, Current-induced spin-orbit torques in ferromagnetic and antiferromagnetic systems, *Rev. Mod. Phys.* **91**, 035004 (2019).
- [2] P. Barla, V. K. Joshi, and S. Bhat, Spintronic devices: A promising alternative to CMOS devices, *J. Comput Electron* **20**, 805 (2021).
- [3] S. Manipatruni, D. E. Nikonov, and I. A. Young, Beyond CMOS computing with spin and polarization, *Nat. Phys.* **14**, 338 (2018).
- [4] J. Sinova, S. O. Valenzuela, J. Wunderlich, C. H. Back, and T. Jungwirth, Spin hall effects, *Rev. Mod. Phys.* **87**, 1213 (2015).
- [5] J. C. R. Sánchez, L. Vila, G. Desfonds, S. Gambarelli, J. P. Attané, J. M. De Teresa, C. Magén, and A. Fert, Spin-to-charge conversion using rashba coupling at the interface between non-magnetic materials, *Nat. Commun.* **4**, 1 (2013).
- [6] S. Karube, K. Kondou, and Y. C. Otani, Experimental observation of spin-to-charge current conversion at non-magnetic Metal/Bi₂O₃ interfaces, *Appl. Phys. Express* **9**, 033001 (2016).
- [7] J. C. Rojas-Sánchez, S. Oyarzún, Y. Fu, A. Marty, C. Vergnaud, S. Gambarelli, L. Vila, M. Jamet, Y. Ohtsubo, A. Taleb-Ibrahimi *et al.*, Spin to Charge Conversion at Room Temperature by Spin Pumping into a New Type of Topological Insulator: α -Sn Films, *Phys. Rev. Lett.* **116**, 096602 (2016).
- [8] H. Tsai, S. Karube, K. Kondou, N. Yamaguchi, F. Ishii, and Y. Otani, Clear variation of spin splitting by changing electron distribution at non-magnetic Metal/Bi₂O₃ interfaces, *Sci. Rep.* **8**, 5564 (2018).
- [9] D. C. Vaz, P. Noël, A. Johansson, B. Göbel, F. Y. Bruno, G. Singh, S. McKeown-Walker, F. Trier, L. M. Vicente-Arche, A. Sander *et al.*, Mapping spin-charge conversion to the band structure in a topological oxide two-dimensional electron gas, *Nat. Mater.* **18**, 1187 (2019).
- [10] C. Sanz-Fernández, V. T. Pham, E. Sagasta, L. E. Hueso, I. V. Tokatly, F. Casanova, and F. S. Bergeret, Quantification of interfacial spin-charge conversion in hybrid devices with a metal/insulator interface, *Appl. Phys. Lett.* **117**, 142405 (2020).
- [11] L. M. Vicente-Arche, J. Bréhin, S. Varotto, M. Cosset-Cheneau, S. Mallik, R. Salazar, P. Noël, D. C. Vaz, F. Trier, S. Bhattacharya *et al.*, Spin-charge interconversion in KTaO₃ 2D electron gases, *Adv. Mater.* **33**, 2102102 (2021).
- [12] V. T. Pham, H. Yang, W. Y. Choi, A. Marty, I. Groen, A. Chuvilin, F. S. Bergeret, L. E. Hueso, I. V. Tokatly, and F. Casanova, Large spin-charge interconversion induced by interfacial spin-orbit coupling in a highly conducting all-metallic system, *Phys. Rev. B* **104**, 184410 (2021).
- [13] G. Allen, S. Manipatruni, D. E. Nikonov, M. Doczy, and I. A. Young, Experimental demonstration of the coexistence of spin hall and rashba effects in β -tantalum/ferromagnet bilayers, *Phys. Rev. B* **91**, 144412 (2015).
- [14] Y. Du, H. Gamou, S. Takahashi, S. Karube, M. Kohda, and J. Nitta, Disentanglement of Spin-Orbit Torques in Pt/Co Bilayers with the Presence of Spin Hall Effect and Rashba-Edelstein Effect, *Phys. Rev. Appl.* **13**, 054014 (2020).
- [15] M. Morota, Y. Niimi, K. Ohnishi, D. H. Wei, T. Tanaka, H. Kontani, T. Kimura, and Y. Otani, Indication of intrinsic spin hall effect in 4d and 5d transition metals, *Phys. Rev. B* **83**, 174405 (2011).
- [16] E. Sagasta, Y. Omori, M. Isasa, M. Gradhand, L. E. Hueso, Y. Niimi, Y. C. Otani, and F. Casanova, Tuning the spin hall effect of pt from the moderately dirty to the superclean regime, *Phys. Rev. B* **94**, 060412(R) (2016).
- [17] J. C. Rojas-Sánchez, N. Reyren, P. Laczkowski, W. Savero, J. P. Attané, C. Deranlot, M. Jamet, J. M. George, L. Vila, and H. Jaffrès, Spin Pumping and Inverse Spin Hall Effect in Platinum: The Essential Role of Spin-Memory Loss at Metallic Interfaces, *Phys. Rev. Lett.* **112**, 106602 (2014).
- [18] W. Zhang, W. Han, X. Jiang, S. H. Yang, and S. S. P. Parkin, Role of transparency of platinum-ferromagnet interfaces in determining the intrinsic magnitude of the spin hall effect, *Nat. Phys.* **11**, 496 (2015).
- [19] C. Pai, Y. Ou, L. H. Vilela-le, D. C. Ralph, and R. A. Buhrman, Dependence of the Efficiency of Spin Hall Torque on the Transparency of Pt/Ferromagnetic Layer Interfaces, *Phys. Rev. B* **92**, 064426 (2015).
- [20] V. T. Pham, M. Cosset-chéneau, A. Brenac, O. Boulle, A. Marty, J. P. Attané, and L. Vila, Evidence of interfacial asymmetric spin scattering at ferromagnet-Pt interfaces, *Phys. Rev. B* **103**, L201403 (2021).
- [21] S. Manipatruni, D. E. Nikonov, C. Lin, T. A. Gosavi, H. Liu, B. Prasad, Y. Huang, E. Bonturim, R. Ramesh, and I. A. Young, Scalable energy-efficient magnetoelectric spin-orbit logic, *Nature (London)* **565**, 35 (2019).
- [22] V. T. Pham, I. Groen, S. Manipatruni, W. Y. Choi, D. E. Nikonov, E. Sagasta, C.-C. Lin, T. A. Gosavi, A. Marty, L. E. Hueso *et al.*, Spin-orbit magnetic state readout in scaled ferromagnetic/heavy metal nanostructures, *Nat. Electron.* **3**, 309 (2020).
- [23] See Supplemental Material at <http://link.aps.org/supplemental/10.1103/PhysRevB.107.184438> for details of enhanced interfacial spin-charge interconversion at an oxidized Cu/W interface, which includes Refs. [37,38].
- [24] Q. Hao, W. Chen, and G. Xiao, Beta (β) tungsten thin films: Structure, electron transport, and giant spin hall effect, *Appl. Phys. Lett.* **106**, 182403 (2015).
- [25] R. J. Pedersen and F. L. Vernon, Effect of film resistance on low-impedance tunneling measurements, *Appl. Phys. Lett.* **10**, 29 (1967).
- [26] J. M. Pomeroy and H. Grube, Negative resistance” errors in four-point measurements of tunnel junctions and other crossed-wire devices, *J. Appl. Phys.* **105**, 094503 (2009).
- [27] E. Sagasta, Y. Omori, S. Vélez, R. Llopis, C. Tollan, A. Chuvilin, L. E. Hueso, M. Gradhand, Y. C. Otani, and F. Casanova, Unveiling the mechanisms of the spin hall effect in Ta, *Phys. Rev. B* **98**, 060410(R) (2018).
- [28] Y. Niimi, M. Morota, D. H. Wei, C. Deranlot, M. Basletic, A. Hamzic, A. Fert, and Y. Otani, Extrinsic Spin Hall Effect Induced by Iridium Impurities in Copper, *Phys. Rev. Lett.* **106**, 126601 (2011).
- [29] Y. Niimi, Y. Kawanishi, D. H. Wei, C. Deranlot, H. X. Yang, M. Chshiev, T. Valet, A. Fert, and Y. Otani, Giant Spin Hall Effect Induced by Skew Scattering from Bismuth Impurities inside Thin Film CuBi Alloys, *Phys. Rev. Lett.* **109**, 156602 (2012).
- [30] P. Laczkowski, Y. Fu, H. Yang, J.-C. Rojas-Sánchez, P. Noel, V. T. Pham, G. Zahnd, C. Deranlot, S. Collin, C. Bouard *et al.*, Large enhancement of the spin hall effect in Au by side-jump scattering on Ta impurities, *Phys. Rev. B* **96**, 140405(R) (2017).

- [31] W. Yan, E. Sagasta, M. Ribeiro, Y. Niimi, L. E. Hueso, and F. Casanova, Large room temperature spin-to-charge conversion signals in a few-layer Graphene/Pt lateral heterostructure, *Nat. Commun.* **8**, 661 (2017).
- [32] Q. Hao and G. Xiao, Giant Spin Hall Effect and Switching Induced by Spin-Transfer Torque in a W/Co₄₀Fe₄₀B₂₀/MgO Structure with Perpendicular Magnetic Anisotropy, *Phys. Rev. Appl.* **3**, 034009 (2015).
- [33] Y. Takeuchi, C. Zhang, A. Okada, H. Sato, S. Fukami, and H. Ohno, Spin-orbit torques in high-resistivity-W/CoFeB/MgO, *Appl. Phys. Lett.* **112**, 192408 (2018).
- [34] K.-U. Demasius, T. Phung, W. Zhang, B. P. Hughes, S.-H. Yang, A. Kellock, W. Han, A. Pushp, and S. S. P. Parkin, Enhanced spin-orbit torques by oxygen incorporation in tungsten films, *Nat. Commun.* **7**, 10644 (2016).
- [35] B. Coester, G. D. H. Wong, Z. Xu, J. Tang, W. L. Gan, and W. S. Lew, Enhanced spin hall conductivity in tungsten-copper alloys, *J. Magn. Magn. Mater.* **523**, 167545 (2021).
- [36] J. Kim, D. Go, H. Tsai, D. Jo, K. Kondou, H. W. Lee, and Y. C. Otani, Nontrivial torque generation by orbital angular momentum injection in ferromagnetic-metal, *Phys. Rev. B* **103**, L020407 (2021).
- [37] E. Villamor, M. Isasa, L. E. Hueso, and F. Casanova, Temperature dependence of spin polarization in ferromagnetic metals using lateral spin valves, *Phys. Rev. B* **88**, 184411 (2013).
- [38] E. Sagasta, Y. Omori, M. Isasa, Y. Otani, L. E. Hueso, and F. Casanova, Spin diffusion length of permalloy using spin absorption in lateral spin valves spin diffusion length of permalloy using spin absorption in lateral spin valves, *Appl. Phys. Lett.* **111**, 082407 (2017).